ACCEPTED VERSION

Ching-Tai Ng and Martin Veidt
Scattering characteristics of Lamb waves from debondings at structural features in composite laminates

*The following article appeared in **J. Acoust. Soc. Am.** 132, 115 (2012) and may be found at* http://dx.doi.org/10.1121/1.4728192

PERMISSIONS

http://acousticalsociety.org/for_authors/posting_guidelines

The Acoustical Society of America (ASA) grants to the author(s) of papers submitted to or published in the *Journal of the Acoustical Society of America (JASA)*, *JASA Express Letters (JASA-EL)* or Proceedings of Meetings on Acoustics (POMA) the right to post and update the article on the Internet with the following specifications.

On the authors' and employers' webpages:

- There are no format restrictions; files prepared and/or formatted by ASA, AIP, or its vendors (e.g., the PDF, PostScript, or HTML article files published in the online journals and proceedings) may be used for this purpose. If a fee is charged for any use of the posted article, ASA permission must be obtained.
- An appropriate copyright notice must be included along with the full citation for the published paper and a Web link to ASA's official online version of the abstract.

25 February 2016

---

http://hdl.handle.net/2440/73270

Scattering characteristics of Lamb waves from debondings at structural features in composite laminates

Ching-Tai Ng [a)]

School of Civil, Environmental & Mining Engineering, The University of Adelaide, Adelaide, SA, 5005, Australia

Martin Veidt

School of Mechanical and Mining Engineering, The University of Queensland, Brisbane, QLD, 4072, Australia

a) Author to whom correspondence should be addressed. Electronic mail: alex.ng@adelaide.edu.au

Abstract

This article investigates the scattering characteristics of Lamb waves from a debonding at a structural feature in a composite laminate. The study specifically focuses on the use of the low frequency fundamental anti-symmetric (A_0) Lamb wave as the incident wave for debonding detection. Three-dimensional (3D) finite element (FE) simulations and experimental measurements are used to investigate the scattering phenomena. Good agreement is obtained between the FE simulations and experimental results. Detailed parameter studies are carried out to further investigate the relationship between the scattering amplitudes and debonding sizes. The results show that the amplitude of the scattered A_0 Lamb wave is sensitive to the debonding size, which indicates the potential of using the low frequency A_0 Lamb wave as the interrogating wave for debonding detection and monitoring. The findings of the study provide improved physical insights into the scattering phenomena, which are important to further advance damage detection techniques and optimise transducer networks.

I. INTRODUCTION

Structural safety is of paramount importance in many engineering fields, including but not limited to civil, mechanical, aerospace and maritime engineering. The safety and integrity of complex structures relies on the performance of individual components as well as their interactions when they are jointed together. The development and use of effective and reliable damage detection techniques improves structural safety while minimising maintenance costs at the same time. Therefore, in the last few decades a variety of damage detection techniques[1-5] have been developed to provide early detection or characterisation of defects in structures.

During this period, it has been shown that Lamb waves have the potential to be a promising method for detecting defects[6-7]. They enable large area inspection, are sensitive to small and different types of defects, and can be used to detect subsurface damages. Their versatility has attracted researchers' attention, and studies have been carried out to investigate Lamb wave scattering characteristics at different types of defects, such as cracks[8], holes[9] and areas of corrosion[10]. The findings of these studies have provided insight into the scattering phenomena of Lamb waves at defects, which is essential to advance the development and optimisation of Lamb wave damage detection techniques and future structural health monitoring systems. The use of Lamb waves to detect defects in simple structures, such as flat isotropic plates, is well developed and a variety of methods[11-15] have been successfully explored. However, damage detection in complex structures such as composite laminates and structures with joints is still a challenging issue.

A. Lamb waves in complex structures

Real structures always contain features, such as joints that connect structural components or reinforcements in order to enhance the structure's performance. Different studies[16-19] have been carried out to investigate the possibility of using Lamb waves to detect defects in complex structures made from isotropic materials. Numerical simulations using finite element (FE) method and experimental measurements have been investigated in the literature.

Dalton *et al.*[20] investigated the performance of Lamb waves as a tool with which to monitor the behaviour and integrity of complex metallic aircraft fuselage components. Different types of structural features, such as double skin, lap and stringer joints, were considered in their study. They concluded that propagating Lamb waves through the entire fuselage was not feasible due to the existence of multiple structural features. Hence, localised monitoring of structurally significant areas was suggested as a practical approach.

Lanza di Scalea *et al.*[21] studied Lamb wave interaction at debonding regions and regions with poorly cured adhesives at bonded lap joints between thin aluminium plates. They showed that the amplitude decrease of selected plate waves leaking from one adhered plate to another through the bondline could be used to detect debonding. Greve *et al.*[22] performed numerical and experimental studies to investigate Lamb waves reflected from cracks at welded joints between steel plates. They showed that a crack could be detected based on the amplitude of the reflected waves.

Schubert[23] presented a survey of using elastodynamic finite integration technique (EFIT) to simulate elastic wave propagation in homogeneous and heterogeneous materials. A number of examples were presented in the survey that shows the feasibility of using EFIT to simulate complicated wave scattering phenomena. Recently, Leckey *et al.*[24] implemented the three-dimensional (3D) EFIT to investigate the Lamb wave scattering at a flat-bottom hole and a void in diffusion bonded aluminium plate. They showed that the 3D simulation can provide additional insight into complicated Lamb wave scattering behaviour.

B. Complex structures made by composite laminates

Fibre-reinforced polymer composite laminates are increasingly employed in different industries due to their light weight, corrosion resistance and high specific stiffness characteristics. However, defects in composite laminates are critical because of the large number of failure modes such as delamination, fibre breaking and matrix or interface fracture. Different studies[25-26] have reported on the scattering characteristics of Lamb waves at defects in laminates and the development of inspection techniques for simple composite

4

structures[27-30]. The research has shown that the propagation and scattering characteristics of Lamb waves at defects in composite laminates are much more complicated than in metallic materials due to the anisotropic nature and multilayer characteristic of the material.

A limited amount of research has investigated the performance and sensitivity of Lamb waves applied to debondings in complex structures constructed of composite laminates. Takeda *et al.*[31] proposed the use of small diameter fibre Bragg grating sensors to measure Lamb waves for damage detection. They showed that the arrival time of Lamb waves transmitted from one side to the other side of a debonding can be used for damage detection. A specimen with a debonding in a double-lap joint was used in the experimental study.

Matt *et al.*[32] studied the strength of transmission of Lamb waves propagating across the skin-to-spar joint to monitor the debonding. A two-dimensional (2D) semi-analytical FE model along with an experimental study were used to confirm the possibility of detecting debonding based on the strength of the transmitted Lamb waves. Lanza di Scalea *et al.*[33] then extended the study, in which the spar was simplified as a multilayer laminate and macro fibre composite transducers were used to actuate and sense the guided waves.

Lissenden *et al.*[34] carried out a study using Lamb waves to detect a debonding at a skin-stringer joint. Numerical and experimental testing was carried out in the study, which employed a simplified 2D composite skin-stringer joint model in which the stringer was modelled as a multilayer laminate.

Damaged composite laminates are regularly repaired by bonding composite patches to restore structural integrity. There are a very limited number of studies focused on this type of structural feature in the literature. Koh *et al.*[35] investigated the possibility of using Lamb waves to assess the integrity of composite repair patches. 2D FE simulations and experimental studies showed that the power transmission of Lamb waves can be used to evaluate the integrity of the repair patches.

Soutis and Diamanti[36] demonstrated the use of Lamb waves to inspect adhesively bonded patch repaired composite laminates. The study specifically focused on the low frequency fundamental anti-symmetric (A_0) Lamb wave. 2D FE simulations and

experimental verifications were carried out in the study. The researchers showed that the change of the low frequency A_0 Lamb wave can be used to detect and locate a debonding between the patch and substrate, and is very sensitive to small changes in the structural integrity of repaired structures.

The aim of this present research study is to investigate the scattering characteristics of the A_0 Lamb wave from a debonding at a structural feature in a composite laminate. The sensitivity of the low frequency incident A_0 Lamb wave to the debonding was assessed quantitatively. Unlike most of the studies in the literature, this research study investigates the 3D characteristics of the A_0 Lamb wave scattering from the debonding in composite laminates. The scattering directivity pattern (SDP) is used to investigate the scattered waves in different directions. Therefore, the numerical and experimental investigations considered in this study are not limited to pure forward and backward scattered waves. The findings are important to further advance and optimise Lamb wave damage detection techniques as well as to design optimal transducer network for future structural health monitoring applications.

The paper first describes the 3D FE simulation of the Lamb waves propagation and scattering from the debonding of a structural feature in Sec. II. The experimental measured data are used to verify the accuracy of the FE simulation in Sec. III. A series of numerical studies using the experimental validated FE model are then carried out to investigate the scattering characteristics of the A_0 Lamb wave from the debonding in Sec. IV. Finally, conclusions are drawn in Sec. V.

II. THREE-DIMENSIONAL FINITE ELEMENT SIMULATIONS

The A_0 Lamb wave propagation and interaction at a debonding in a [45/-45/0/90]s quasi-isotropic (QI) composite laminate with a structural feature was simulated using a 3D explicit FE method. The 3D FE modelling was performed using commercial FE software ANSYS/LS-DYNA. Eight-noded 3D reduced integration solid brick elements with hourglass control were used in the model, in which each node has three degrees of freedom (x, y and z displacements). A schematic diagram of the FE model is shown in Fig. 1.

The length and width of the QI composite laminate model in the x and y directions of the Cartesian coordinate system shown in Fig 1b were 180 mm and 240 mm, respectively. The [45/-45/0/90]$_S$ QI composite laminate was constructed from 0.2 mm thick Cycom 970/T300 unidirectional carbon/epoxy prepreg tape for each lamina. The thickness of the base composite laminate was 1.6 mm. Each lamina was modelled as an orthotropic material. The effective elastic properties were determined using micromechanics theory, taking the constituent materials into consideration. The fibre volume fraction and density were 0.55 and 1517 kg/m^3, respectively. In the composite laminate FE model, each lamina was modelled by a single layer of solid brick elements with the effective elastic properties as shown in Table I.

The structural feature was modelled as a multilayer laminate, which had the same laminate layup as the base laminate, but was placed on top of the base laminate as shown in Fig 1b. The structural feature was used to represent bonded doublers, skin-stringer joints or basic composite laminate repairs. As discussed in Sec. I.B, a number of studies have modelled these joints and repaired composite laminates using similar approaches[33-36]. As shown in Fig 1, the centre of a 22 mm wide structural feature was located at $x =$ 0 mm. The length of the structural feature in the y direction is the same as the base composite laminate. Fig 1b shows a sketch of the cross section through the debonding in the x-z plane. It is assumed that the structural feature and base laminate are co-cured during the manufacturing process, hence, no additional adhesive layer is included in the model.

A rectangular debonding between the structural feature and base laminate (between 8th and 9th lamina) was modelled by separating the FE nodes across the debonding surfaces at the debonding region. A similar modelling approach was used and experimentally validated to model delamination damage[25].

The A$_0$ Lamb wave was excited by applying nodal displacement in the out-of-plane z direction to the surface nodes located at $z = 0.8$ mm simulating a piston type excitation by a 5 mm diameter half circle transducer as shown in Fig 1a. The transducer was located at $x =$ -90 mm and $y =$ 0 mm. A 140 kHz narrow band six-cycle sinusoidal tone burst pulse modulated by a Hanning window was used as the excitation signal. At this low frequency,

only the fundamental symmetric (S_0), shear horizontal (SH_0) and A_0 can exist in the composite panel. The wavelength λ of the A_0 Lamb wave in the composite laminate is 7.93 mm, which is the smallest wavelength among these three fundamental Lamb wave modes at the excitation frequency. Most of the solid brick elements had in-plane square shapes with dimensions 0.4 mm $\times$ 0.4 mm, but the elements near the half circle transducer had a slight variation in size and shape. This very fine FE mesh ensures that at least 17 FE nodes exist per wavelength of the A_0 Lamb wave[25]. As the wavelength of the A_0 Lamb wave is much smaller than S_0 and SH_0 at the excitation frequency, the 3D FE model is also able to accurately predict the S_0 and SH_0 Lamb waves, which may be induced due to the mode conversion effect at the debonding.

Figs 2a and 2b show that typical 3D snapshots of the FE simulated out-of-plane displacement of the A_0 Lamb wave interacting with the structural feature without and with the debonding, respectively. It should be noted that Fig 2 shows the wave field at the same time of two different simulations. Both figures show that there exist complex reflected and transmitted wave fields from the structural feature, which are different for the panels without and with debonding. The reflected wave from the debonding at the structural feature is more complicated than the reflected wave from a delamination[25] or a through hole[26] in a flat panel, in which the existence of the defect creates a reflected wave, which does not exist in an undamaged panel. This implies that baseline measurements are more difficult for extracting the scattered wave from the debonding at the structural feature for damage detection purposes.

III. EXPERIMENTAL VALIDATION

This section presents an experimental verification of the 3D FE model described in Sec. II. The subsection III.A first presents the details of the experimental setup. A comparison of the experimentally measured data and the FE simulations is then given in subsection III.B.

A. Experimental setup

Two 600 mm × 600 mm composite laminates with a structural feature were manufactured using Cycom® 970/T300 unidirectional carbon/epoxy prepreg tape. The stacking sequence of the composite laminate was [45/-45/0/90]$_S$, the same as the FE model described in Sec. II. Fig 3 shows the composite laminate specimen with the structural feature, which was a 22 mm × 600 mm [45/-45/0/90]$_S$ composite laminate strip attached on the top of the base laminate along the middle of the panel in $\theta = 90°$ direction.

During the manufacturing process, the base laminate and structural feature were co-cured in an autoclave with metal caul plates at 700 kPa and 180°C following the standard cure cycle for the aerospace material. Hence no adhesive was used to join the structural feature to the base laminate. A 12 mm × 12 mm and a 22 mm × 22 mm square debonding were generated by inserting fluorinated ethylene propylene separator films between the interface of the structural feature and base laminate (8th and 9th lamina in Fig 1b) in two composite laminates, respectively.

Ferroperm Pz27 piezoceramic disc actuators of 5 mm diameter and 2 mm thickness were bonded to the surface of the composite laminate. A 3 mm thick brass backing mass with the same diameter was used to increase the strength of the A_0 Lamb wave and minimise the unwanted S_0 Lamb wave. The excitation signal was a 140 kHz narrow band six-cycle sinusoidal tone burst pulse modulated by a Hanning window, which is the same as the excitation signal used in the FE simulations in Sec. II. A computer controlled arbitrary waveform generator [Stanford Research DS345 (Sunnyvale, California, USA)] with a 10 V peak-to-peak output voltage was used to generate the excitation signal. The signal was then amplified by a factor of 10 − 50 using a power amplifier [Krohn Hite model 7500 (Brockton, Massachussets, USA)].

The scattered Lamb wave was measured by a Laser Doppler vibrometer [OFV 303/OFV 3001, Polytech GmbH (Waldbronn, Germany)]. The laser head was positioned by a computer controlled positioning system [Newport ESP 300 (Irvine, California, USA)]. The laser head was perpendicular to the surface of the panel to ensure that only the out-of-plane

displacement component was measured. As the out-of-plane displacement of the S_0 mode is much smaller than the A_0 mode Lamb wave[37], the unwanted S_0 Lamb waves, which may be excited by the transducer or created by mode conversion at the structural feature, were minimised to have a negligible magnitude in the measurements. Thin reflective tapes were surface mounted to the measurement locations on the composite laminate to enhance the optical backscatter reflection of the laser beam.

B.   Transmitted Lamb waves at debonding

In this section of the paper the 3D FE scattering model is validated by comparing the FE simulation results and the experimentally measured data. The specimen described in Sec. III. A was used in the validation. The FE simulation of the incident A_0 Lamb wave propagation was experimentally verified for the base composite laminate with respect to the directivity excitation amplitude, group velocity[26] and phase velocity[25].

The focus of this section is on the verification of the interaction of the interrogating wave with the intact and debonded structural feature. As discussed in Sec. II, baseline measurements are essential for extracting the scattered wave fields from the debonding damage. However, the debonding was generated during the manufacturing process, which means the baseline measurements of the intact panel are not available. Comparing the reflected and transmitted waves in Figs 2a and 2b, the transmitted waves are less complex and have larger amplitude change for the debonded panel. Hence the experimental verification focuses on the transmitted wave amplitudes.

For each composite laminate specimen, measurements were taken at five different locations ($r = $ 40 mm, and $\theta = $ 0°, 20°, 40°, 320° and 340°). Fig 4 shows the experimentally measured and FE simulated transmitted waves at $r = $ 40 mm and $\theta = $ 0° in the panel without and with the 12 mm $\times$ 12 mm debonding at the structural feature. The width of the debonding is the same as the width of the structural feature. Solid and dashed lines represent the signal obtained from panel without and with the debonding. For the experimental study, the signal for the panel without the debonding was obtained at another

location in the same panel. Good agreement is obtained between the experimental measurements and FE simulations, especially on the arrival time of the transmitted waves, and the amplitude difference and phase change of the transmitted waves of the composite laminate without and with the debonding. Fig 4 shows that the amplitude of the transmitted wave from the panel with the debonding at the structural feature is obviously much higher than that in the intact panel. This is because the debonding, which is across the total width of the structural feature, separates the structural feature and the base laminate. Hence, the incident wave can completely by-pass the structural feature at $\theta = 0°$. This phenomenon significantly differs from the scattering behaviour at through holes or delaminations in flat composite laminates, in which the amplitude of the transmitted wave is reduced due to the existence of defects[25-26]. The experimental measurements have more pronounced mode coupling compared to FE simulations. This is evidenced by small wave packets in the experimental measurements in Fig 4. It is because the experimental results were measured at the surface of the panel using Laser Doppler vibometer while the FE simulations results were obtained by monitoring the out-of-plane nodal displacement at FE nodes located at the mid-thickness of the panel.

Figs 5a and 5b provide a quantitative comparison between the experimental measurements and FE simulations for the panel with the 12 mm × 12 mm and the 22 mm × 22 mm debonding, respectively. The calculations for the figures are based on the maximum amplitude of the transmitted wave envelopes for different θ using the Hilbert transform analysis[38-39]. The FE simulation results of the transmitted wave amplitudes for the panel without and with the debonding, and the difference between these two amplitudes, are indicated by solid, dash and dash-dotted lines, respectively. The corresponding results from the experimental measurements are represented by circles, crosses and triangles. They show that there is a reasonable agreement between the FE and experimental results on the transmitted wave amplitude patterns for the panel with and without the debonding. As shown in Fig 5, the experimental measured wave amplitudes are generally smaller than the FE simulations. In the case of the transmitted wave amplitudes for panel without the debonding

(solid lines and circles), it may be caused by the matrix rich area at the interface between the base laminate and the structural feature in the specimens. For the panel with the debonding, the discrepancy between the FE (dashed lines) and experimental (crosses) results may be caused by the inserted fluorinated ethylene propylene propylene separator films which were not modelled in the FE simulations. However, a very good agreement is obtained between the FE and the experimental results for the difference between the amplitude of the wave transmitted from the panel with and that without the debonding (dash-dotted lines and triangles). This demonstrates that the FE simulation is able to accurately predict the amplitude change of the transmitted waves due to the debonding.

IV. Scattered A_0 Lamb wave and scattering directivity pattern

The accuracy of the 3D FE simulation was demonstrated using the experimental data presented in Sec. III. The validated 3D FE model was used to study the A_0 Lamb wave scattering characteristics at the debonding. As the focus here was mainly on the A_0 Lamb wave, two FE simulations with identical FE mesh for the panel with and without the debonding were required in order to isolate the scattered A_0 Lamb wave from the incident wave and waves reflected from the boundaries of the composite laminate. The A_0 scattered Lamb wave can be calculated by[26]

$$u_{r,\theta}^{(S)}\left(t\right) = u_{r,\theta}^{(D)}\left(t\right) - u_{r,\theta}^{(U)}\left(t\right) \tag{1}$$

where r and θ are the radial and azimuthal coordinates of the cylindrical coordinate system shown in Fig 1a. $u_{r,\theta}^{(S)}(t)$ is the out-of-plane displacement components of the extracted scattered Lamb waves at location r and θ, and time t. $u_{r,\theta}^{(D)}(t)$ and $u_{r,\theta}^{(U)}(t)$ are the out-of-plane displacement components of the Lamb waves for the panel with and without the debonding, respectively. It should be noted that the A_0 Lamb wave is obtained by monitoring the out-of-plane nodal displacement at particular nodes located at the mid-thickness of the laminate. This ensures that only the A_0 Lamb wave is extracted from the simulated results as the S_0 and SH_0 Lamb waves have zero out-of-plane displacement at the mid-thickness of the laminate.

The SDP can then be calculated by determining the maximum amplitude of signal envelop of $\hat{u}_{r,\theta}^{(S)}(t)$, which is obtained using Hilbert transform[38-39], at all monitoring nodes, which form a circular measurement with the centre located at the centroid of the debonding. In this study, the out-of-plane displacements were taken at 36 monitoring nodes located at r = 40 mm and $0° \leq \theta \leq 360°$ with 10° increments. It should be noted that the SDP is normalised by the maximum amplitude of the incident wave envelope at the debonding centre location of the intact laminate.

Using the experimentally verified 3D FE scattering model and the aforementioned approach, the scattered A_0 Lamb wave and the SDP can then be calculated for debondings of different sizes. The dimension of the debondings was parameterised by d_x and d_y, which represent the debonding width and length in the x and y directions, respectively. A convenient way to present the results for different sizes of debondings is to normalise the d_x and d_y to the wavelength of the A_0 incident wave at $\theta = 0°$, which is consistent with most scattering work, as

$$D_x = d_x / \lambda \quad \text{and} \quad D_y = d_y / \lambda \tag{2}$$

where D_x and D_y are defined as debonding size to wavelength ratio. These ratios provide the possibility ot generalise the results to different damage sizes.

Figs 6a, 6b and 6c show the SDPs for the 22 mm × 12 mm, 22 mm × 17 mm and 22 mm × 22 mm debonding, respectively, the corresponding debonding size to wavelength ratios are D_x = 2.77, and D_y = 1.51, 2.14 and 2.77, respectively. The size of the debonding in the y axis increases from Figs 6a to 6c while the size in the x axis remains unchanged. All three figures show that the energy of the scattered wave is mainly concentrated in the forward and backward directions. The forward scattering energy is larger than the backward scattering energy, for a larger D_y. However, the scattering amplitudes around the directions perpendicular to the incident wave have a relatively small magnitude. Fig 6 also shows that the SDP is not symmetric with respect to the 0° direction for symmetrical rectangular debondings. The reasons for this are that the excited A_0 Lamb wave amplitude is not symmetric with respect to the 0° direction, and the scattered wave amplitude is influenced by

13

the fibre orientation of the outer laminae of the composite laminate[26].

Figs 7a and 7b show the SDP for the debonding with $D_y = 2.77$, and $D_x = 1.51$ and 2.14, respectively. Comparing Figs 7a, 7b and 6c, in which the debondings have the same value of D_y but with different values of D_x, the amplitude of the scattered wave again mainly concentrates on forward and backward directions.

A. Influence of debonding size

It has been demonstrated through the SDP that the scattered wave mainly concentrates on the forward and backward directions. This section explores the influence of the debonding size on the scattering characteristics in detail. Debondings with different d_y are investigated while d_x remains unchanged. Figs 8a and 8b show the normalised forward and backward amplitudes as a function of D_y, respectively, while the value of the D_x is unchanged and equal to 2.77. Fig 8a shows the normalised forward scattering amplitudes at $\theta = 0°$, 30°, 60°, 300° and 330° as a function of D_y. For $\theta = 0°$, the amplitudes first rise and then start falling when D_y is around 0.63. For D_y larger than approximately 0.88, the values increase and have the largest amplitude comparing to the other θ directions at $D_y = 2.77$. For $\theta = 30°$ and 330°, the normalised amplitudes increase and reach the local maximum at around $D_y = 0.50$. The values then fluctuate around a slightly increasing trend line. For $\theta = 60°$ and 300°, the normalised amplitudes exhibit a slight variation without increase.

Fig 8b shows the normalised backward scattering amplitudes at $\theta = 120°$, 150°, 180°, 210° and 240°. Overall, the normalised backward scattering amplitudes are smaller than the forward scattering amplitudes, especially at $\theta = 180°$ for larger D_y. The normalised backward scattering amplitudes at $\theta = 180°$ behave differently for D_y larger by around 0.5, with amplitudes increasing linearly at a much slower rate.

Fig 9 shows the normalised forward and backward amplitudes as a function of D_x. The figure considers the effect of increasing the debonding size in the x direction until the debonding width is the same as the width of the structural feature. As opposed to Fig 8, the forward and backward scattering amplitude characteristics of Fig 9 have less fluctuation. Fig

9a shows the normalised forward amplitudes at $\theta = 0°$, $30°$, $60°$, $300°$ and $330°$. The normalised forward scattering amplitudes at $\theta = 0°$ always have a larger amplitude compared to the amplitudes of the other θ directions. The amplitude at $\theta = 0°$ has the maximum at $D_x = 2.65$. After that the normalised amplitude drops to 1.97 at $D_x = 2.77$, for which the structural feature is completely debonded in the x direction. The normalised forward scattering amplitudes at $\theta = 30°$ and $330°$ have very similar values and rise linearly for larger D_x. However, the normalised forward scattering amplitudes are much smaller than the amplitudes of $\theta = 0°$. At $\theta = 60°$ and $300°$ the overall trend is a very slow increase.

Fig 9b shows the normalised backward scattering amplitudes at $\theta = 120°$, $150°$, $180°$, $210°$ and $240°$. The backward scattering amplitudes at $\theta = 180°$ and $210°$ have similar characteristics and the overall backward scattering amplitude at $\theta = 180°$ is larger than that at $\theta = 210°$. The amplitudes rise and reach the maximum value at around $D_x = 1.40$. After that the backward amplitudes fall and start increasing at around $D_x = 2.27$ and 2.14 for $\theta = 180°$ and $210°$, respectively. The backward scattering amplitudes at $\theta = 120°$, $150°$ and $240°$ exhibit a slight variation but the overall trend is a slow increase. As shown in Figs 8 and 9, the scattering amplitudes generally have small magnitudes in oblique directions. In terms of detecting the debonding, these directions are not suitable locations for sensing the scattered waves.

B. Influence of debonding location

The investigations reported in the previous section showed that the Lamb wave scattering characteristics are highly dependent on the size of the debonding. It is obvious that the scattering characteristics also depend on the debonding location. This section investigates the influence of debonding locations on the forward and backward scattering amplitudes. The square debondings with $D_x = D_y = 1.26$ and centroid located at 84 mm $\leq x \leq 96$ mm and $y = 110$ mm are considered. The size of the debondings is 10 mm $\times$ 10 mm, smaller than the width of the structural feature (22 mm). Fig 10 shows the normalised forward and backward scattering amplitudes as a function of the centroid location of the debonding in the x axis.

The figure shows that the normalised scattering amplitudes at $\theta = 0°$ and $180°$ have a very similar magnitude to the debondings located at $x = 84$ mm and 96 mm, located to the left and right ends of the structural feature, respectively. For the debonding located within the structural feature, the scattering amplitudes at $\theta = 0°$ and $180°$ fluctuate around a nearly horizontal trend line and the forward scattering amplitudes at $\theta = 0°$ always have a larger amplitude than the backward scattering amplitudes at $\theta = 180°$.

V. CONCLUSIONS

The characteristics of A_0 Lamb wave scattering from a debonding in a composite laminate structural feature were investigated in this study. 3D FE simulations and experimental measurements were used to demonstrate that the 3D FE scattering model is able to accurately predict the A_0 Lamb wave scattering from the debonding.

The study shows that the reflected wave from the debonding at the structural feature is much more complicated than that from defects in simple composite laminates. The baseline measurements are essential to extract the scattered waves for damage detection purpose. The transmitted wave characteristics, in which the amplitudes increase because of the debonding, are completely different to the case of the defects in simple composite laminates. Detailed parameter studies have shown that both forward and backward scattering amplitudes are of the same order of magnitude for the small debonding sizes. However, the forward scattering amplitudes dominate for larger debonding sizes. The scattered waves in directions forming a large angle with the incident wave, the scattering amplitudes are always small.

The research study has also shown that the amplitude of the scattered A_0 Lamb wave is sensitive to the debonding size and the debonding location within the structural feature. This shows the potential of employing the A_0 Lamb wave to identify the size and monitor the growth of the debonding. Potential applications include monitoring debonding at structural joints and repair patches in composite laminates. In addition, the findings are important to further advance damage detection techniques and optimise transducer networks.

REFERENCES

[1] H. Sohn, C.R. Farra, F.M. Hemez, J.J. Czarnecki, D.D. Shunk, D.W. Stinemates, B.R. Nadler, A review of Structural Health Monitoring Literature: 1996 – 2001, Report Number LA-13976-MS (Los Alamos National Laboratory, Los Alamos, NM, 2004), total pages, 301.

[2] H.F. Lam, C.T. Ng, A.Y.T. Leung, "Multi-crack detection on semi-rigidly connected beams utilizing transient vibration data following probabilistic approach," J. Eng. Mech, ASCE **134**, 90 – 99 (2007).

[3] B. Xu, V. Giurgiutiu, "Single mode tuning effects on Lamb wave time reversal with piezoelectric wafer active sensors for structural health monitoring," J. Nondestr. Eval. **26**, 123 – 134 (2007).

[4] H.F. Lam, C.T. Ng, "The selection of pattern features for structural damage detection using an extended Bayesian ANN algorithm," Eng. Struct. **30**, 2762 – 2770 (2008).

[5] C.T. Ng, M. Veidt, H.F. Lam, "Guided wave damage characterisation in beams utilising probabilistic optimisation," Eng. Struct. **31**, 2842 – 2850 (2009).

[6] J.L. Rose, "A baseline and vision of ultrasonic guided wave inspection potential," J. Pressure Vessel Technol. **124**, 273-282 (2002).

[7] A. Raghavan, C.E.S. Cesnik, "Review of guided-wave structural health monitoring," Shock and Vib. Digest **39**, 91 – 114 (2007).

[8] M. Ratassepp, M.J.S. Lowe, P. Cawley, A. Klauson, "Scattering of the fundamental shear horizontal mode in a plate when incident at a through crack aligned in the propagation direction of the mode," J. Acoust. Soc. Am. **124**, 2873 – 2882 (2008).

[9] P. Fromme, M.B. Sayir, "Measurement of the scattering of a Lamb wave by a through hole in plate," J. Acoust. Soc. Am. **111**, 1165 – 1170 (2002).

[10] L. Moreau, A. Velichko, P.D. Wilcox, "Accurate finite element modelling of guided wave scattering from irregular defects," NDT&E International **45**, 46 – 54 (2012).

[11] L.R.F. Rose, C.H. Wang, "Mindlin plate theory for damage detection: Source solutions," J.

Acoust. Soc. Am. **116**, 154 – 171 (2002).

[12] P. Wilcox, "Omi-directional guided wave transducer arrays for the rapid inspection of large areas of plate structures," IEEE Trans. Ultrason. Ferroelectr. Freq. Control **50**, 699 – 709 (2003).

[13] P.S. Tua, S.T. Quek, Q. Wang, "Detection of cracks in plates using piezo-actuated Lamb waves," Smart Mater. Struct. **13**, 643 – 660 (2004).

[14] C.H. Wang, J.R. Rose, F.K. Chang, "A synthetic time-reversal imaging method for structural health monitoring," Smart Mater. Struct. **13**, 415 – 423 (2004).

[15] M. Veidt, C.T. Ng, S. Hames, T. Wattinger, "Imaging laminar damage in plates using Lamb wave beamforming," Adv. Mater. Res. **47-50**, 666 – 669 (2008).

[16] S.I. Rokhlin, "Lamb wave interaction with lap-shear adhesive joints: theory and experiment," J. Acoust. Soc. Am. **89**, 2758-2765 (1991).

[17] A. Guillet, M. Kettani, F. Luppe, "Guided waves' propagation in an elastic plate of linearly varying thickness," J. Acoust. Soc. Am. **105**, 1340 (1999).

[18] Mal, Z. Chang, D. Guo, "Lap joint inspection using plate wave," In Proceedings SPIE **2945**, 128 – 137 (1996).

[19] M.J.S. Lowe, R.E. Challis, C.W. Chan, "The transmission of Lamb waves across adhesively bonded lap joints," J. Acoust. Soc. Am. **107**, 1333 – 1345 (2000).

[20] R.P. Dalton, P. Cawley, M.J.S. Lowe, "The potential of guided waves for monitoring large areas of metallic aircraft fuselage structure," J. Nondestr. Eval. **20**, 29 – 45 (2001).

[21] F. Lanza di Scalea, M. Bonomo, D. Tuzzeo, "Ultrasonic guided wave inspection of bonded lap joints: noncontact method and photoelastic visualization," Res. Nondestr. Eval. **13**, 153 – 171 (2001).

[22] D.W. Greve, N. Tyson, I.J. Oppenheim, "Interaction of defects with Lamb waves in complex geometries," IEEE Ultrasonics Symposium **1**, 297 – 300 (2005).

[23] F. Schubert, "Numerical time-domain modelling of linear and nonlinear ultrasonic wave propagation using finite integration techniques – theory and applications," Ultrasonics **42**,

221 – 229 (2004).

[24] C.A.C. Leckey, M.D. Rogge, C.A. Miller, M.K. Hinders, "Multiple-mode Lamb wave scattering simulations using 3D elastodynamic finite integration technique," Ultrasonic **52**, 139 – 207 (2012).

[25] C.T. Ng, M. Veidt, "Scattering of the fundamental anti-symmetric Lamb wave at delaminations in composite laminate," J. Acoust. Soc. Am. **129**, 1288 – 1296 (2011).

[26] M. Veidt, C.T. Ng, "Influence of stacking sequence on scattering characteristics of the fundamental anti-symmetric Lamb wave at through holes in composite laminates," J. Acoust. Soc. Am. **129**, 1280 – 1287 (2011).

[27] K. Diamanti, J.M. Hodgkinson, C. Soutis, "Detection of low-velocity impact damage in composite plates using Lamb waves," Struct. Health Monitor. **3**, 33 – 41 (2004).

[28] C.T. Ng, M. Veidt, N. Rajic, "Integrated piezoceramic transducers for imaging damage in composite laminates," Proceedings of SPIE **7493**, 74932M (2009).

[29] L.R.F. Rose, C.H. Wang, "Mindlin plate theory for damage detection: imaging of flexural inhomogeneities," J. Acoust. Soc. Am. **127**, 754 – 763 (2010).

[30] A. Srivastava, F. Lanza di Scalea, "Quantitative structural health monitoring by ultrasonic guided waves," J. Eng. Mech. ASCE. **136**, 937 – 944 (2010).

[31] N. Takeda, Y. Okabe, J. Kuwahara, S. Kojima, T. Ogisu, "Development of smart composite structures with small-diameter fiber Bragg grating sensors for damage detection: quantitative evaluation of delamination length in CFRP laminates using Lamb wave sensing," Compos. Sci. Technol. **65**, 2575 – 2587 (2005).

[32] H. Matt, I. Bartoli, F. Lanza di Scalea, "Ultrasonic guided wave monitoring of composite wing skin-to-spar bonded joints in aerospace structures," J. Acoust. Soc. Am. **118**, 2240 – 2252 (2005).

[33] F. Lanza di Scalea, H. Matt, I. Bartoli, S. Coccia, G. Park, C. Farrar, "Health monitoring of UAV wing skin-to-spar joints using guided waves and macro fiber composite transducers," J. Intell. Mater. Syst. Struct. **18**, 373 – 388 (2007).

[34] C.J. Lissenden, P.K. Puthillath, J.L. Rose, "Guided wave feature identification for monitoring structural damage in joints between composite laminates," Mater. Forum **33**, 279 − 285 (2009).

[35] Y.L. Koh, W.K. Chiu, N. Rajic, "Integrity assessment of composite repair patch using propagating Lamb waves," Compos. Struct. **58**, 363 − 371 (2002).

[36] C. Soutis, K. Diamanti, "A Lamb wave based SHM of repaired composite laminated structures," 2nd International Symposium on NDT in Aerospace **We.2.B.1**, 1 − 10 (2010).

[37] F. Lanza di Scalea, P. Rizzo, "Propagation of ultrasonic guided waves in lap-shear adhesive joints: Case of incident a0 Lamb wave," J. Acoust. Soc. Am. **115**, 146 − 156 (2004).

[38] W.J. Staszewski, C. Boller, G. Tomlinson, *Health Monitoring of Aerospace Structures: Smart Sensor Technologies and Signal Processing* (John Wiley & Sons, Inc., West Sussex, UK, 2004), pp. 163 − 206.

[39] C.T. Ng, M. Veidt, "A Lamb-wave-based tech*nique for damage detection in composite laminates," Smart Mater. Struct. **18**, 1 − 12 (2009).*

LIST OF TABLES

TABLE I. Effective material properties of Cycom® 970/T300 prepreg lamina

E_{11} (GPa)	128.75
E_{22} (GPa)	8.35
E_{33} (GPa)	8.35
G_{12} (GPa)	4.47
G_{13} (GPa)	4.47
G_{23} (GPa)	2.90
ν_{12}	0.33
ν_{13}	0.33
ν_{23}	0.44
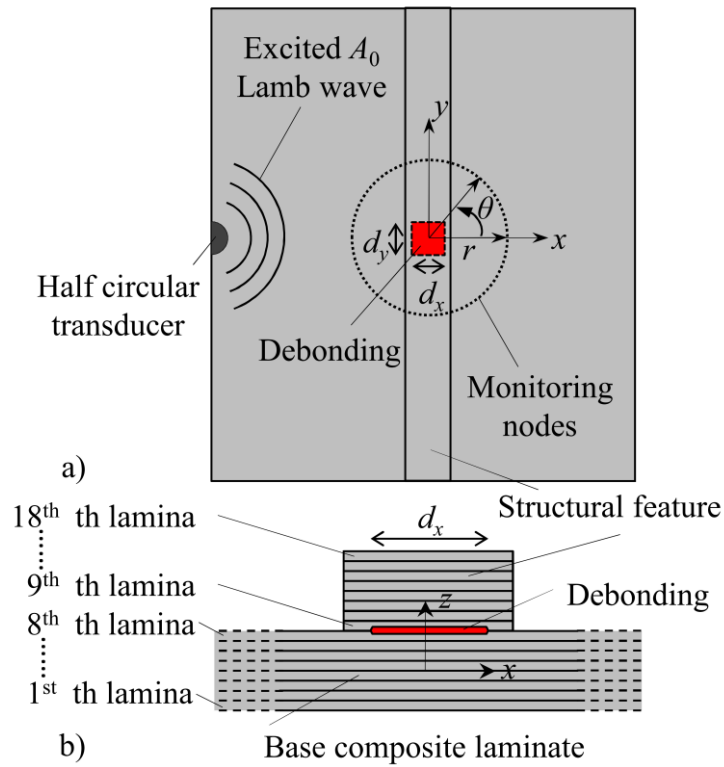
FIG 1. a) Schematic diagram of the configuration used in the FE simulations and b) zoom-in of the cross section through the debonding (Colour online)
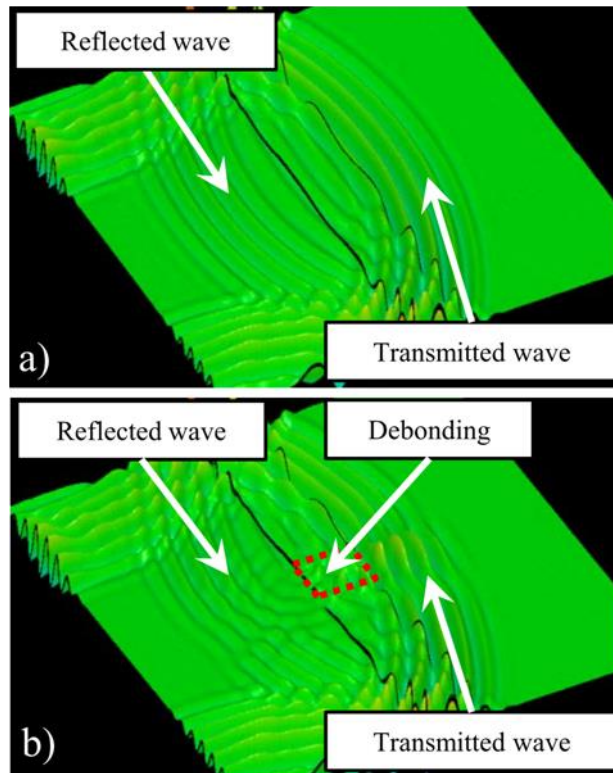

FIG 2 Typical 3D snapshots of the FE simulated out-of-plane displacement at shortly after the A_0 Lamb wave interacting at the structural feature a) without and b) with the debonding (Colour online)
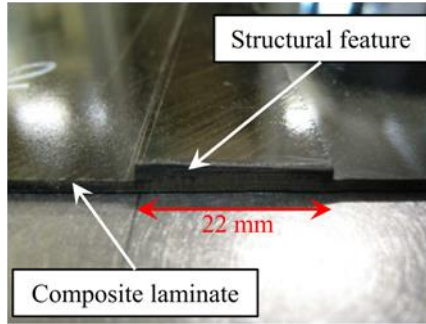
FIG 3. a) Specimen of the composite laminate with the structural feature (Colour online)
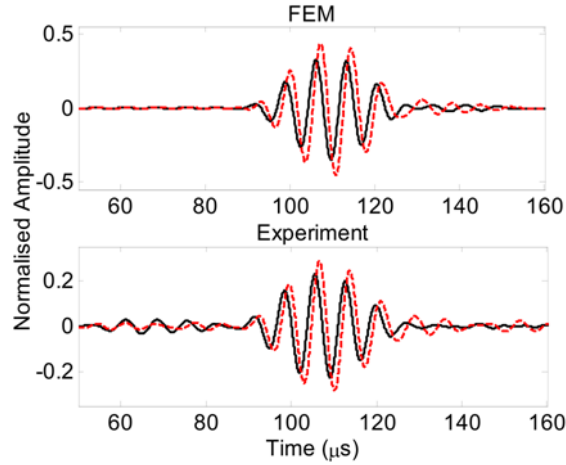
FIG 4. Transmitted waves at $r = 40$ mm and $\theta = 0°$, of the panel with a 12 mm $\times$ 12 mm debonding at the structural feature (solid line: without debonding; dash line: with debonding) (Colour online)
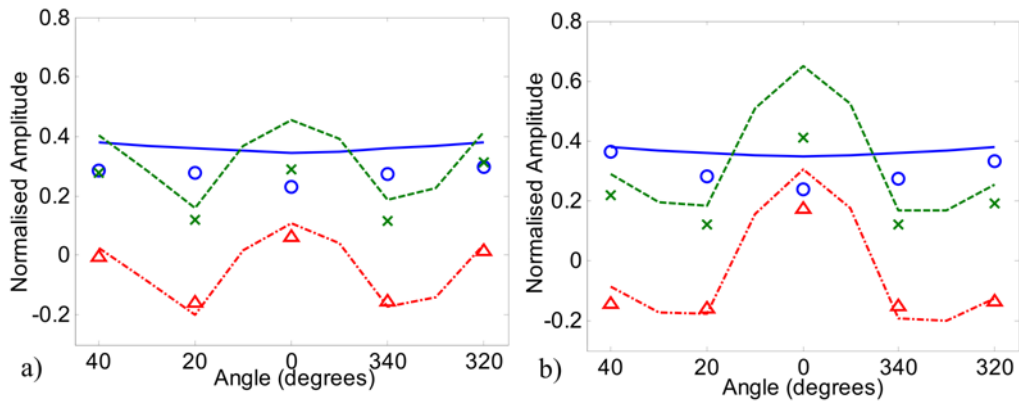
FIG 5. Transmitted wave amplitudes, amplitude differences between panels without and with the a) 12 mm $\times$ 12 mm and b) 22 mm $\times$ 22 mm debonding (solid line, FE baseline data; dash line, FE debonding data; dash-dot line, difference between data of panel with and without debonding in FE simulation; circles, experimental baseline data; crosses experimental debonding data; triangles, difference between data of panel with and without debonding in experiment) (Colour online)
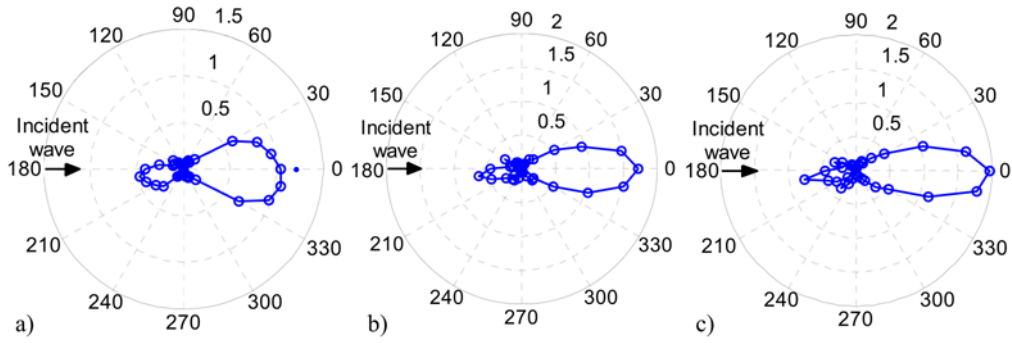
FIG 6. FE simulation results of SDP for the debonding with $D_x = 2.77$, and $D_y =$ a) 1.51, b) 2.14 and c) 2.77 (Colour online)
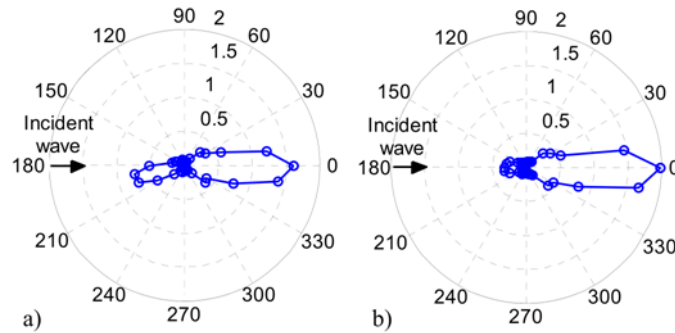

FIG 7. FE simulation results of SDP for the debonding with $D_y = 2.77$, and $D_x =$ a) 1.51 and b) 2.14 (Colour online)
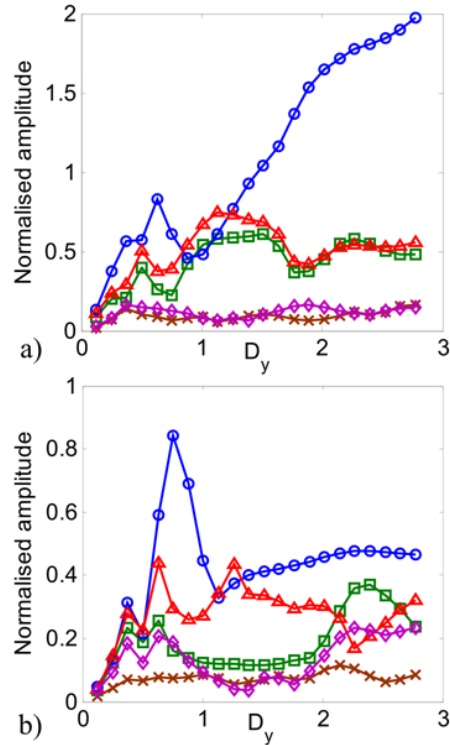

FIG 8. FE simulation results of normalised a) forward (circles, $\theta = 0°$; squares, $\theta = 30°$; crosses, $\theta = 60°$; rhombus, $\theta = 300°$; triangles, $\theta = 330°$) and b) backward scattering amplitudes (crosses, $\theta = 120°$; squares, $\theta = 150°$; circles, $\theta = 180°$; triangles, $\theta = 210°$; rhombus, $\theta = 330°$) as a function of D_y with $D_x = 2.77$ (Colour online)

24

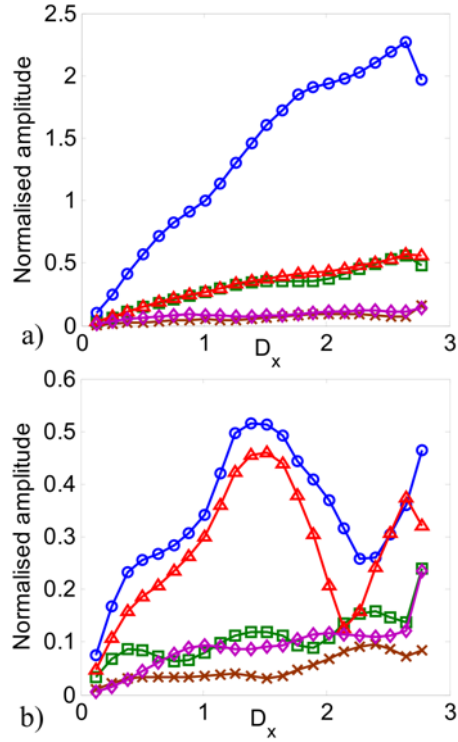FIG 9. FE simulation results of normalised a) forward (circles, $\theta = 0°$; squares, $\theta = 30°$; crosses, $\theta = 60°$; rhombus, $\theta = 300°$; triangles, $\theta = 330°$) and b) backward scattering amplitudes (crosses, $\theta = 120°$; squares, $\theta = 150°$; circles, $\theta = 180°$; triangles, $\theta = 210°$; rhombus, $\theta = 330°$) as a function of D_x with $D_y = 2.77$ (Colour online)
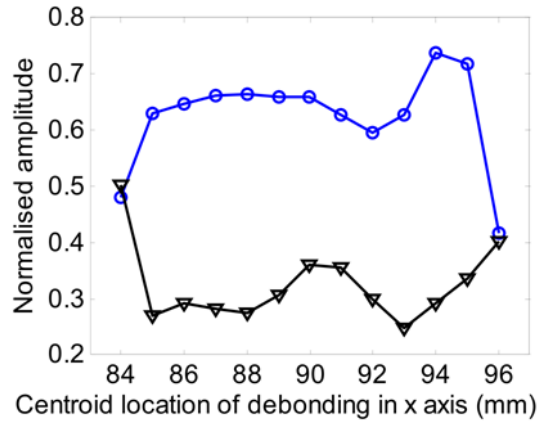

FIG 10. FE simulation results of normalised amplitude forward (circles, $\theta = 0°$) and backward scattering amplitudes (triangles, $\theta = 180°$) as a function of the debonding location ($D_x = D_y = 1.26$) in x axis (Colour online)

25